JOURNAL OF APPLIED CRYSTALLOGRAPHY
ISSN 1600-5767

Evolution of texture and internal stresses within polycrystalline rock salt using *in situ* 3D synchrotron computed tomography and 3D X-ray diffraction

Amirsalar Moslehy,[a]* Khalid A. Alshibli,[a] Timothy J. Truster,[a] Peter Kenesei,[b] Wadi H. Imseeh,[a] Zaher Jarrar[a] and Hemant Sharma[b]

[a]Civil and Environmental Engineering, University of Tennessee, 851 Neyland Drive, 325 John D. Tickle Engineering Building, Knoxville, TN 37996, USA, and [b]Advanced Photon Source (APS), Argonne National Laboratory, 9700 South Cass Avenue, Lemont, IL 60439, USA. *Correspondence e-mail: amoslehy@vols.utk.edu

Received 3 December 2020
Accepted 29 July 2021

Edited by H. Brand, Australian Synchrotron, Australia

Keywords: X-ray diffraction; lattice strain; rock salt crystal structure; grain stress; halite microstructure.

Rock salt caverns have been extensively used as reliable repositories for hazardous waste such as nuclear waste, oil or compressed gases. Undisturbed rock salt deposits in nature are usually impermeable and have very low porosity. However, rock salt formations under excavation stresses can develop crack networks, which increase their porosities; and in the case of a connected crack network within the media, rock salt may become permeable. Although the relationship between the permeability of rock salt and the applied stresses has been reported in the literature, a microscopic study that investigates the properties influencing this relationship, such as the evolution of texture and internal stresses, has yet to be conducted. This study employs *in situ* 3D synchrotron micro-computed tomography and 3D X-ray diffraction (3DXRD) on two small-scale polycrystalline rock salt specimens to investigate the evolution of the texture and internal stresses within the specimens. The 3DXRD technique measures the 3D crystal structure and lattice strains within rock salt grains. The specimens were prepared under 1D compression conditions and have shown an initial {111} preferred texture, a dominant $\{110\}\langle 1\bar{1}0\rangle$ slip system and no fully connected crack network. The {111} preferred texture under the unconfined compression experiment became stronger, while the $\{111\}\langle 1\bar{1}0\rangle$ slip system became more prominent. The specimens did not have a fully connected crack network until applied axial stresses reached about 30 MPa, at a point where the impermeability of the material becomes compromised due to the development of multiple major cracks.

1. Introduction

Caverns within rock salt deposits or domes have been used as reliable storage for various materials for many years (Senseny *et al.*, 1992; Carter *et al.*, 1993; Staudtmeister & Rokahr, 1997; Fam *et al.*, 1998; Cosenza *et al.*, 1999; Zhu & Arson, 2014; Bauer & Urquhart, 2016). Recently, designing containerless storage caverns for compressed air or gas has gained more attention (Zeljaś, 2016; Zhang *et al.*, 2017; Wang *et al.*, 2018). However, switching to a containerless storage design emphasizes the importance of the low porosity and impermeability of the material used for storage. Rock salt's physical and mechanical properties, such as low porosity, low permeability, ductility and self-healing, make it a viable choice for containerless storage (Yin *et al.*, 2019, 2020; Sun *et al.*, 2019; Habibi, 2019; Liu *et al.*, 2019; Chen *et al.*, 2020). In low-porosity materials such as compressed polycrystalline rock salt, the existence of a connected pore network controls the permeability of the rock mass. Therefore, the development of

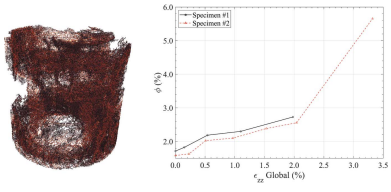

a connected pore network within the rock salt formation affects the serviceability of rock salt storage. Undeformed polycrystalline rock salt with porosities below a critical value ranging from 0.02 to 0.05 usually does not have a connected pore network (Paneru *et al.*, 2018). The distribution of stresses within rock salt under loading can initiate and propagate cracks and result in an undesirable connected pore network. In addition, the initial texture of polycrystalline materials influences the development of the pore network within them (Ding *et al.*, 2014). The anisotropic response of rock salt grains to the applied stresses is highly dependent on the initial texture of the polycrystalline rock salt deposit. Rock salt has a face-centered cubic (f.c.c.) crystal structure [Fig. 1(*a*)]. Crystals with an f.c.c. structure have a set of six primary slip systems along the {110} planes and $\langle 1\bar{1}0\rangle$ directions [Fig. 1(*b*)]. Additionally, f.c.c. crystal structures have six secondary slip systems along {100} planes in the directions of ⟨011⟩ [Figs. 1(*c*)] and 12 secondary slip systems along {111} planes in the directions of $\langle 1\bar{1}0\rangle$ [Fig. 1(*d*)].

Depending on the ambient conditions and tectonic pressures at which a rock salt deposit has been compressed, it might develop a preferred crystal orientation (texture). Skrotzki & Welch (1983) studied rock salt's texture development during halokinesis, the process of salt formations flowing towards the surface under tectonic forces (Talbot, 1978), by conducting extrusion tests on natural rock salt blocks. A circular billet was forced through a conical die containing the rock salt specimen, applying a uniaxial stress up to 700 MPa on the core being extruded. The texture of the specimens was then identified using neutron diffraction. Specimens extruded at room temperature or below showed strong ⟨111⟩ and ⟨115⟩ fibers, while specimens extruded at higher temperatures exhibited a dominant ⟨100⟩ fiber. However, the texture can develop differently depending on the direction of the applied stresses. Lebensohn *et al.* (2003) investigated the evolution of plastic deformations and texture in synthetic polycrystalline rock salt. The texture of the compacted specimens was found to be uniform. The specimens were then tested in extensional triaxial experiments, and their texture after the deformation was evaluated using the electron beam scattering pattern method. The deformed specimens were found to have strong texture components of both {100} and {111}. The abundance of grains with {100} orientations was due to the fact that these grains had a higher probability of slipping on {110}⟨110⟩, resulting in significant plastic deformations of the grains. The deformed grains could then recrystallize and grow to form a dominant {100} texture. Linckens *et al.* (2016) tested natural rock salt single-crystal specimens using the unconfined compression procedure at a strain rate of 10^{-7} s^{-1} to investigate the initiation of deformation mechanisms. The stresses were applied perpendicular to {100} planes to facilitate the activation of the {110}⟨110⟩ slip system. Light and scanning electron microscopy were used to examine the activation of the mentioned slip system. The major deformation mechanism was found to be dislocation creep through the formation of sub-grains caused by activating the {110}⟨110⟩ slip system. Although plastic deformations within rock salt can result in crack propagations, not all components of plastic deformations contribute to it. Na & Sun (2018) employed a crystal plastic and a multi-phase field-based approach to simulate the anisotropic thermomechanical response of single-crystal rock salt. They found, by separating the strains of the individual grains into volumetric and deviatoric strains and then only considering the deviatoric strains, that the predicted crack propagation within the specimen converges with the actual crack propagation.

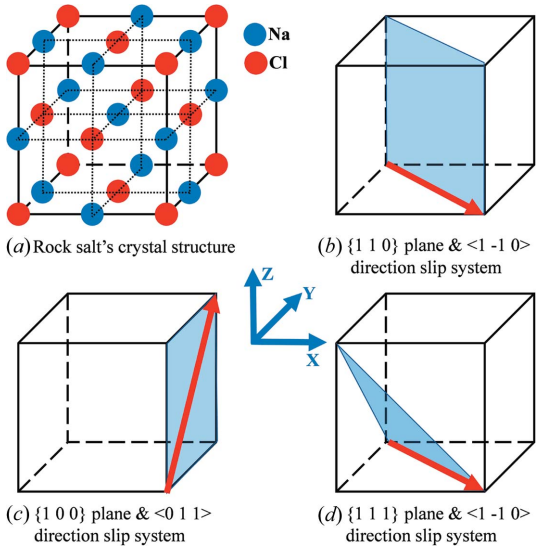

Figure 1
Rock salt's crystal structure and its primary and secondary slip systems.

Intact rock salt formations usually have low porosity and permeability; however, local cracks may develop during excavation and drilling activities which can significantly increase the permeability of rock salt (Schulze *et al.*, 2001). Popp *et al.* (2001) investigated the relationship between wave velocity, permeability and porosity of natural polycrystalline rock salt specimens in hydrostatic compaction and compressional and extensional triaxial experiments. Specimens tested in hydrostatic loading up to 30 MPa did not show any dilatancy, and their permeability decreased by more than ten times compared with the original cores. The decrease in the permeability of the specimens was due to the closure of microcracks formed by the coring process used to collect them. The specimens tested in triaxial experiments had a dilatancy onset at a differential stress of about 12 MPa. The permeability of the specimens was found to increase upon reaching the dilatancy onset. However, the specimens did not show significant crack propagation until the differential stresses reached between 18 and 30 MPa (corresponding to axial strains between 5 and 15%), where the increase in the permeability reached a constant plateau. The findings showed that the cracks mainly formed along {100} planes of the grains, and their orientations with respect to the specimen were highly influenced by the loading path, which caused an anisotropic permeability in the specimens. Alkan (2009) developed a percolation model describing the relationship between the dilatancy and permeability of rock salt at stresses

caused by excavation. The specimens were tested under compression triaxial conditions and the development of cracks within the specimens was investigated by microscopy after the test. The main dislocation of the grains was found to be in the direction of the major principal stress (σ_1), causing the permeability to increase in this direction. The specimens showed a dilatancy boundary approximately at σ_1 = 22 MPa, where the micro-fractures within the specimen formed an interconnected pore network resulting in a significant spike in permeability. On the other hand, under high hydrostatic stresses, the deformations may result in complete closure of the cracks within rock salt formations. Singh *et al.* (2018) studied the deformations caused by boring cavities inside polycrystalline rock salt deposits. The specimens showed preferred orientation on ⟨100⟩ and ⟨110⟩ when tested in triaxial compression for the purpose of model verification. The results prove that if the lateral earth pressure is high enough (*e.g.* if the depth of the cavity is greater than 1000 m), the visco-elasto-plastic deformations over a span of 10 years can close the opening entirely.

Computed tomography (CT) has been proven to be a suitable nondestructive technique to capture the crack network and its evolution within rock salt (Keller *et al.*, 2014; Thiemeyer *et al.*, 2015). However, the sole usage of CT does not provide any insights regarding the evolution of stresses or texture within rock salt specimens. A solution to overcome this shortcoming is the utilization of electron backscatter diffraction (EBSD) scanning on representative sections of the specimen (Lebensohn *et al.*, 2003). EBSD can only scan the surface of the specimen or, if used to capture scans inside the specimen, it becomes a destructive method; therefore, it cannot be employed in conjunction with mechanical testing methods. As a result, EBSD can only reveal the texture of the specimen after mechanical tests, such as an unconfined compression test, and it cannot track the evolution of texture or stresses inside the specimen. 3D X-ray diffraction (3DXRD) is a nondestructive *in situ* technique that can measure the development of texture and internal stresses of a crystalline material composed of thousands of grains (Sharma *et al.*, 2012*a*,*b*; Hurley *et al.*, 2016, 2018; Imseeh & Alshibli, 2018; Amirrahmat *et al.*, 2020; Imseeh *et al.*, 2020). In 3DXRD, an incident X-ray beam is targeted at the crystalline specimen. The incident beams diffract when they reach the crystal planes of the grains of the specimen. The diffracted beams follow Bragg's law [Fig. 2(*a*)],

$$2d_{hkl}\sin\theta_{hkl} = \lambda, \qquad (1)$$

where *hkl* is the crystal plane (*hkl*) with Miller indices of *h*, *k* and *l*, d_{hkl} is the distance between two consecutive *hkl* planes, θ_{hkl} is the diffraction angle, and λ is the wavelength of the incident beam. When the incident X-ray beam diffracts from the (*hkl*) plane, it forms Debye–Scherrer rings on a detector placed behind the specimen [Fig. 2(*b*)]. Therefore, by having the values of λ and θ_{hkl}, the interplanar distance of d_{hkl}, which is directly related to the lattice parameters of a crystal, can be calculated. By measuring the lattice parameters of a crystal under various applied stresses, the lattice strains of a crystal can be calculated throughout an experiment. The rotation of a polycrystalline specimen about the loading axis allows the diffraction patterns of different (*hkl*) planes of each crystal to be collected, which eventually yields the strain matrix of individual crystals.

Borthwick, Schmidt, Piazolo, Gundlach, Griera *et al.* (2012) employed an *in situ* 3DXRD technique in annealing experiments conducted on a melt-grown single-crystal rock salt specimen. The specimen was heated to 400°C and a subvolume of it was mapped by 3DXRD scans before and after annealing. The sub-grain boundary misorientations changed during the annealing process, though they did not show a clear decreasing or increasing pattern. Moreover, a clear trend of sub-grain sub-division was observed within the areas that did not exhibit misorientations before. Furthermore, Borthwick, Schmidt, Piazolo & Gundlach (2012) compared the previously obtained results from *in situ* 3DXRD during the annealing of the specimen with the results obtained from *in situ* EBSD scans obtained from the same specimen. The analyses of the EBSD scans confirmed all the findings from the 3DXRD scans regarding the changes in sub-grain misorientations and sub-grain subdivision. However, the sub-grain boundary migration rates found using the 3DXRD scans were significantly higher. This discrepancy shows that 2D EBSD scans cannot fully capture grain/sub-grain boundary migration. Viganò & Ludwig (2018) and Viganò *et al.* (2016) proposed the implementation of diffraction contrast tomography, a 3DXRD technique coupled with CT, for determining grain and grain

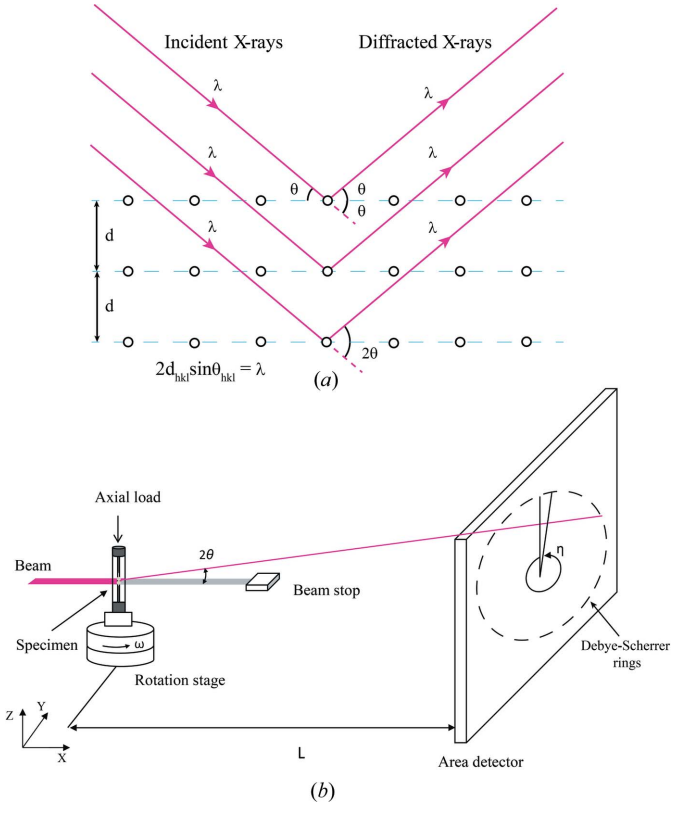

Figure 2
(*a*) Bragg's law, (*b*) 3DXRD setup (Alshibli *et al.*, 2013).

boundary characteristics such as crystallographic orientation in polycrystalline rock salt. The specimen was composed of large NaCl grains and fine-sized Cu particles as a contrast agent. A sub-volume of the specimen containing about 300 grains was successfully scanned and reconstructed. The spatial positions of the mapped grains and their crystallographic orientations were more accurate than those collected from EBSD scans captured for verification.

In summary, there have been many studies on the evolution of porosity and cracks or the development of internal stresses and texture within polycrystalline rock salt under loading. However, no study has yet examined the evolution of all the aforementioned properties at the same time and their interrelationships in rock salt specimens under applied loads. This paper studies the evolution of cracks, porosity, texture and internal stresses in polycrystalline rock salt under an unconfined loading condition. Moreover, the internal stresses developed within the specimens are compared with the stresses applied at the specimens' boundaries. Two polycrystalline rock salt specimens were prepared in this study by dry compression of salt grains. They were tested under the unconfined compression procedure coupled with *in situ* 3DXRD and synchrotron micro-computed tomography (SMT) measurements. The SMT scans were analyzed by image processing procedures to track the porosity and crack network of the specimens throughout the experiments. The 3DXRD scans were used for evaluating the internal stresses and orientations of the grains within a sub-volume of the specimen during the experiments containing more than 10 000 grains.

2. Experiments

2.1. Specimen preparation

The raw salt grains used to prepare the specimens for this study were sourced from Windsor Salt Mine, Ontario, Canada. The original prismoidal rock salt block obtained from the mine was about 1.5 × 1.5 × 0.3 m, and it was cut into smaller specimens for various experiments. Rock salt grains needed for preparing small-scale specimens were prepared by grinding larger single-crystal specimens into a grain size smaller than 0.075 mm (sieve No. 200). The nominal water content of the ground grains prior to specimen preparation was found to be 0.1% according to ASTM D2216-19 (2019). The specimen preparation method was inspired by the procedure of Moslehy & Alshibli (2021) for preparing dry polycrystalline rock salt specimens; however, the specimens prepared in this study are significantly smaller in size, enabling them to be scanned by a typical synchrotron X-ray beam. Rock salt grains were deposited in three equal layers into a nylon tube that had an inner diameter (ID) of 1.66 mm and a wall thickness of 0.76 mm, such that the tube could be extruded without the need to apply excessive axial stresses directly to the specimen. The nylon tube was placed inside a cylindrical acrylic die with an ID of 3.18 mm, a wall thickness of 14.29 mm and a length of 38.10 mm to withhold axial stresses of more than 200 MPa [Fig. 3(*a*)]. Each layer of the grains was compressed at an axial stress of 200 MPa at room temperature for 20 s. At the end of the compression of the last layer, the specimen was additionally compressed for 1 h using the same axial stress. The specimen was then extruded and annealed at a temperature of 200°C for 7 days. Fig. 3(*b*) shows a photograph of specimen No. 1 after the annealing process. The specimens were not perfectly cylindrical, and the edges of the top and bottom of the specimens were elevated [Fig. 3(*b*)]. Considering the small size of the specimens, the ends could not be ground using conventional specimen mounting techniques without introducing damage to the specimens; however, precision lapping fixtures can be employed in future studies for mounting and grinding specimens of this size. The dimensions and weight of the specimens were measured, and their initial porosities were calculated assuming a specific gravity of 2.17 for the rock salt grains (Table 1).

Table 1
Physical properties of the specimens after annealing, and crystal properties of rock salt grains calculated from P-XRD results.

Specimen	Height (mm)	Diameter (mm)	Weight (g)	Porosity (%)
1	2.32	2.04	0.0162	1.6
2	2.51	2.01	0.0170	1.6

Property	Value
Chemical formula	NaCl
Crystal system	f.c.c.
Lattice system	f.c.c.
Space-group No.	225
Space-group name	$Fm\bar{3}m$
Unit-cell lattice parameters	$a = b = c = 5.6386$ Å, $\alpha = \beta = \gamma = 90°$
Volume	179.27 Å^3
Calculated density	2.165 g cm^{-3}

The crystal properties of the constituent grains of the specimens are a key input in determining the properties of the grains being scanned using the *in situ* 3DXRD technique. Therefore, a representative amount of the ground grains was evaluated using the powder X-ray diffraction (P-XRD)

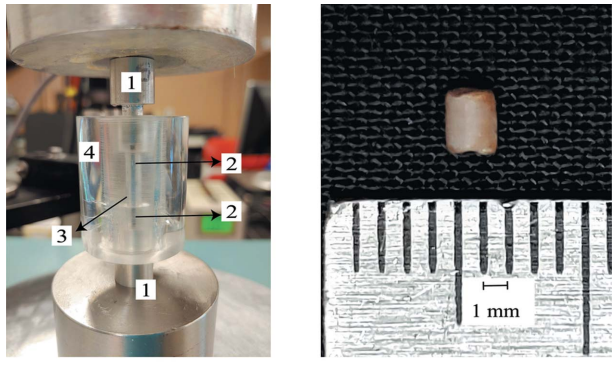

(*a*) 1. End plates
2. Loading rods attached to the end plates
3. Nylon tube
4. Acrylic die

(*b*)

Figure 3
Polycrystalline rock salt specimen preparation: (*a*) the compression setup; (*b*) specimen No. 1 after the 1D compression and annealing.

method. The grains were scanned by a PANalytical Empyrean diffractometer using $K\alpha_1$ beams generated from a copper tube and the diffraction pattern was captured using a PIXcel3D detector. Additionally, the instrument was calibrated by performing P-XRD on LaB_6 standard reference material in accordance with the NIST standard (Black *et al.*, 2011) to eliminate the instrumental errors. Phase identification was initially conducted on the diffraction pattern using the *High-Score* suite (Degen *et al.*, 2014). The collected pattern was a 99.9% match to the halite's powder diffraction file (PDF). The collected pattern was then refined by the full Rietveld procedure (McCusker *et al.*, 1999) using *GSAS II* (Toby & Von Dreele, 2013) based on Swanson and Fuyat's standard halite diffraction pattern (Swanson & Fuyat, 1953). The calculated crystal properties of the rock salt grains used in this study are presented in Table 1.

2.2. Unconfined compression test with *in situ* SMT and 3DXRD

The unconfined compression tests in this study were conducted using a special compression apparatus designed by Druckrey & Alshibli (2016) with a minor modification. The apparatus is a small-scale servo automated load frame capable of applying axial loads up to 1700 N. The bottom part of the cell is stationary and houses a load cell. The axial forces are applied by a stepper motor placed on the top part of the test cell. The top part of the load frame is mounted by four acrylic rods on the bottom part. These provide access to the loading platens, but they do not interfere significantly with X-ray beams due to their low mass attenuation. The 4 mm-diameter loading platens are made of tungsten to prevent any indentation by the samples being tested [Fig. 4(*a*)]. The apparatus can be operated in both stress- and strain-controlled modes, where the deformations are obtained from the stepper motor applying the axial load. The specimens were tested in a strain-controlled mode at a constant displacement rate of 0.0009 mm s^{-1}, resulting in a constant strain rate of $\sim 4 \times 10^{-4}$ s^{-1}. In addition to the initial SMT and 3DXRD scans, loading was paused at predetermined strains to acquire the SMT and 3DXRD scans. The test on specimen No. 1 was paused at 0.15, 0.54, 1.10 and 1.98% axial strains while the test on specimen No. 2 was paused at 0.23, 0.51, 0.97, 1.53, 2.04 and 3.32% axial strains.

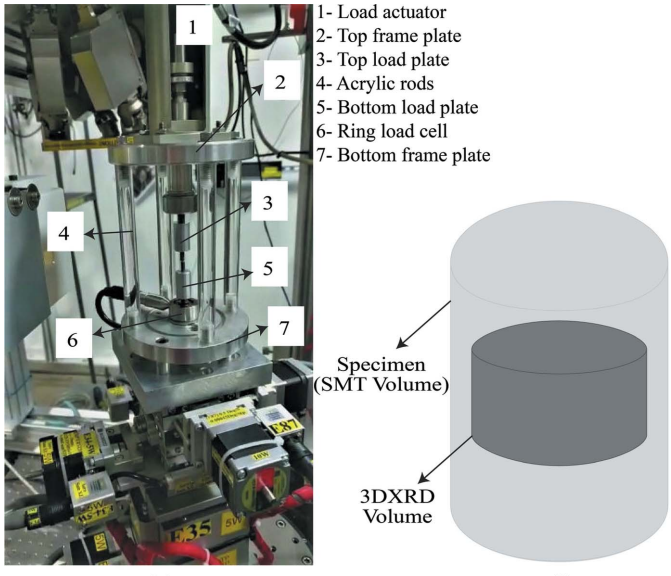

Figure 4
(*a*) The unconfined compression apparatus; (*b*) the volume scanned in the 3DXRD measurements; (*c*) *in situ* SMT–3DXRD setup at beamline 1-ID, APS, ANL.

The *in situ* SMT and 3DXRD measurements were acquired using X-ray beamline 1-ID at the Advanced Photon Source (APS), Argonne National Laboratory (ANL), Illinois, USA. Fig. 4(*c*) shows the test cell setup on the beamline stage. SMT scans were acquired in two stacks, each measuring 2.1 mm (width) × 1.3 mm (height). The cell was rotated 360° at 0.25° increments with an exposure time of 0.9 s, which produced a total of 2304 2D SMT radiographs with a spatial resolution of 1.17 µm per pixel. The 2D scans were processed using *tomoRecon* code (Rivers, 2012). The 3DXRD scans were acquired in three layers; each scan used a beam that measured 2.1 mm (width) × 0.4 mm (height) on a sub-volume of the specimens at 0.1° rotation increments scanning more than 10 000 grains. Fig. 4(*b*) shows the position of the sub-volume of the specimens scanned using the 3DXRD beam. The 3DXRD scans were analyzed by *Microstructural Imaging Diffraction Analysis Software* (*MIDAS*) (Sharma *et al.*, 2012*a*,*b*). *MIDAS* calculates various properties of the grains of the specimens being scanned including, but not limited to, unit-cell lattice parameters, spatial coordinates with respect to the specimen's coordinate system, orientation matrices with respect to the specimen's coordinate system and lattice strains.

3. Results and discussion

3.1. Global strength behavior of the specimens

Fig. 5 shows the relationship between the global axial strain (ϵ_{zz}) and the global axial stresses (σ_{zz}). The black diamonds and red squares show ϵ_{zz} where SMT and 3DXRD scans were acquired. The ϵ_{zz} values were initially obtained from the displacements derived by the rotational displacement of the stepper motor. The elevated edges of the specimens were crushed with the increase in the applied global σ_{zz}, resulting in artificially high ϵ_{zz} (six to seven times higher than expected) even when they were adjusted using the displacements obtained from the SMT scans. The final adjusted ϵ_{zz} were obtained by tracking traceable micro-cracks within the speci-

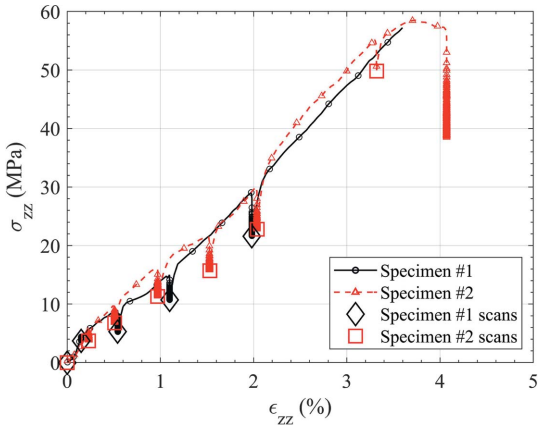

Figure 5
Global axial strain versus global axial stress during the unconfined compression experiments.

mens located at the top and the bottom of the specimens in the SMT scans at different strain steps. These micro-cracks were selected at a distance of two times the height of the elevated edges towards the center of the specimens in the loading direction (z) to avoid the stress fluctuations caused by the elevated edges. The cross-sectional area used in calculating σ_{zz} was also initially calculated according to equation (2), as per ASTM D2850-15 (2015) and ASTM D4767-11 (2020) standards, which is valid only under an unconfined compression condition and assuming there is no volume change within the specimen:

$$A = \frac{A_0}{(1-\epsilon_{zz})}, \tag{2}$$

where A_0 is the initial cross-sectional area and A is the adjusted cross-sectional area of the specimen at ϵ_{zz}. Equation (2) accounts for the increase in the cross-sectional area of the specimens with the increase in the axial load. Although the estimated A calculated by equation (2) is usually considered accurate, the assumption of no volume changes within the specimens might not be valid in all instances. Furthermore, the SMT scans provide a much more accurate measurement of the cross-sectional area of the specimens throughout the experiments. Therefore, the cross-sectional area of the specimens was additionally adjusted using the SMT scans.

The unconfined compressive strength of specimen Nos. 1 and 2 is very close to that of the dry compressed specimens and dry annealed specimens reported by Moslehy & Alshibli (2021). The dry compressed specimens reported by Moslehy & Alshibli (2021) were not annealed at all, while the dry annealed specimens were annealed under their compression stresses for 7 days. However, specimen Nos. 1 and 2 in this study were annealed without any applied stresses for 7 days. The average unconfined compressive strength of specimen Nos. 1 and 2 (~59 MPa) was skewed towards the unconfined compressive strength of the dry compressed specimens. The grains of the dry compressed specimens were found to be less recrystallized compared with the dry annealed specimens. Moreover, the grain boundaries of the dry compressed specimens were not diffused, in contrast to those of the dry annealed specimens. Therefore, this similarity to the dry compressed specimens shows that, in the absence of applied stresses during the annealing process in the preparation of specimen Nos. 1 and 2, the grains did not have the opportunity to fully recrystallize, and their grain boundaries did not have the chance to significantly diffuse during specimen preparation.

Specimen Nos. 1 and 2 showed higher strains prior to failure than the dry compressed specimens. The aforementioned imperfections (such as the elevated edges) of specimen Nos. 1 and 2, even considering the remedies used to remove their adverse effects on the calculated strains, resulted in larger displacements (strains) being calculated. Also, the applied stresses on the specimens were paused multiple times during the tests, which resulted in the creep and relaxation of the specimens, enabling them to undergo more deformations. Lastly, recrystallization and grain boundary diffusion led to the material behaving in a more ductile way, resulting in higher strains (Moslehy & Alshibli, 2021).

3.2. Evolution of the texture and internal stresses within the grains

MIDAS measures the orientations of the scanned grains in 3DXRD with respect to the specimen axes at each 3DXRD measurement. The orientation of each grain was then processed by the orientation matrix defined in equation (3), which transforms the grain's coordinate system into the specimen's global coordinate system:

$$\mathbf{R} = \begin{bmatrix} a_{xx} & a_{xy} & a_{xz} \\ a_{yx} & a_{yy} & a_{yz} \\ a_{zx} & a_{zy} & a_{zz} \end{bmatrix}, \tag{3}$$

where a_{xi}, a_{yi} and a_{zi} define the [100], [010] and [001] directions of the grain with respect to the specimen global coordinate system. The orientations of the grains obtained from *MIDAS* were then converted to Bunge Euler angles by solving the following:

$$\mathbf{R}^{\mathrm{T}} = \begin{bmatrix} \cos\varphi_1 \cos\varphi_2 - \sin\varphi_1 \sin\varphi_2 \cos\Phi & \sin\varphi_1 \cos\varphi_2 + \cos\varphi_1 \sin\varphi_2 \cos\Phi & \sin\varphi_2 \sin\Phi \\ -\cos\varphi_1 \sin\varphi_2 - \sin\varphi_1 \cos\varphi_2 \cos\Phi & -\sin\varphi_1 \sin\varphi_2 + \cos\varphi_1 \cos\varphi_2 \cos\Phi & \cos\varphi_2 \sin\Phi \\ \sin\varphi_1 \sin\Phi & -\cos\varphi_1 \sin\Phi & \cos\Phi \end{bmatrix}, \tag{4}$$

where φ_1, Φ and φ_2 are the counterclockwise rotation angles of the specimen's axes about the z axis, the [100] direction and the [001] direction, respectively, to transfer the specimen axes to the crystal axes. The Euler angles of the grains were then used to define the orientation distribution function (ODF) of the specimens using the *MTEX* MATLAB toolbox (Hielscher

& Schaeben, 2008). The obtained ODF results were employed to investigate the changes in the specimens' texture. Fig. 6 shows the texture of the specimens with respect to the z axis of the specimens at different ϵ_{zz} measured in multiples of random distribution (MRD). Both specimens exhibited a strong texture along the {111} orientation before the test [Figs. 6(*a*) and 6(*f*)]; however, specimen No. 1 exhibited a strong texture along {035} as well. Moreover, specimen No. 2 showed a stronger presence of {001} texture whereas specimen No. 1 showed a very low presence of {001} texture. These findings demonstrate that rock salt specimens prepared by the 1D compression method have an initially preferred texture on the {111} orientation which contrasts with the conventional assumption of having an initial random texture (Lebensohn *et al.*, 2003; Liu *et al.*, 2005).

Specimen No. 1 developed a stronger texture along the {111} orientation and the {035} texture diminished with increasing σ_{zz}. Moreover, the {035} texture moved towards the {011} texture in addition to the previously mentioned {111} texture during the experiment. The increase in the intensity of the {111} texture is a clear indication that the {111}⟨1$\bar{1}$0⟩ slip system had been the dominant active slip system within the grains (Lebensohn *et al.*, 2003). Specimen No. 2 likewise developed a stronger texture about the {111} orientation,

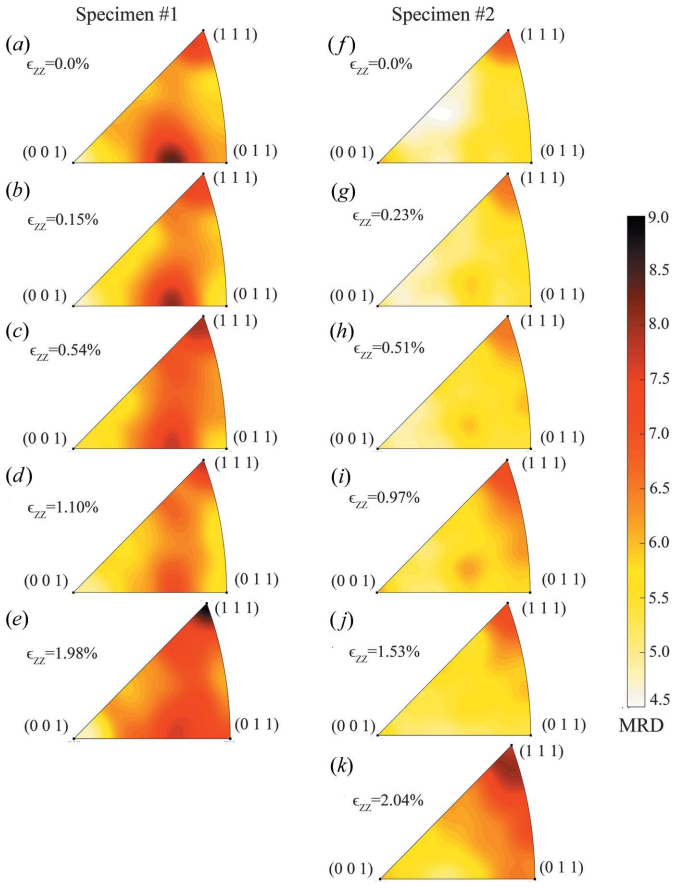

Figure 6
The evolution of texture within the specimens with respect to the z axis at different global axial strains: (*a*)–(*e*) specimen No. 1; (*f*)–(*k*) specimen No. 2.

which shows the potential high activity of the {111}⟨1$\bar{1}$0⟩ slip system. The presence of the {111} texture within the specimens before the tests could increase the activity of the {111}⟨1$\bar{1}$0⟩ slip system in comparison with the other slip systems, whereas rock salt specimens without any initial texture usually show more activity of the {110}⟨1$\bar{1}$0⟩ slip system at room temperature (Linckens *et al.*, 2016). Additionally, specimen No. 2 evolved a moderate texture towards the {011} orientation. The increase in the {011} texture (Goss texture) of the specimens during the experiments could be a direct result of grain migration and rotation, where instead of the interior/space diagonal of the grains being parallel to the z axis of the specimen, their face diagonals became parallel to the z axis of the specimen. In other words, the grain edges became dominant in the plane perpendicular to the specimen's z axis rather than the two vertices connecting the grain's space diagonal. The initial texture found after the 1D compression loading used in the specimen preparation can be utilized to calibrate numerical models in lieu of assuming a random initial texture for the material. Moreover, the development of texture for the unconfined compression experiments can be employed in the validation of future numerical models, which eventually leads to better prediction of the response of the material.

MIDAS also calculates the lattice strains that occurred within the grains at any given strain in the specimen coordinates system using Bragg's law as explained earlier. The general form of the lattice strains for a grain is

$$\boldsymbol{\epsilon} = \begin{bmatrix} \epsilon_{xx} & \epsilon_{xy} & \epsilon_{xz} \\ \epsilon_{yx} & \epsilon_{yy} & \epsilon_{yz} \\ \epsilon_{zx} & \epsilon_{zy} & \epsilon_{zz} \end{bmatrix}, \tag{5}$$

where ϵ_{ij} is the strain on a plane with a normal vector parallel to the i axis, towards the j axis. To calculate the stresses of the grains from their strains, the strains needed to be defined in the coordinate system of the individual grains. The strains of the grains in their own coordinate system ($\boldsymbol{\epsilon}'$) were calculated using equation (6):

$$[\boldsymbol{\epsilon}'] = [\mathbf{R}][\boldsymbol{\epsilon}][\mathbf{R}^{\mathrm{T}}]. \tag{6}$$

Further, using the Voigt notation and the stiffness matrix ($\mathbf{C}$) of rock salt, the stresses of the grains in their own coordinate system ($\boldsymbol{\sigma}'_{\mathrm{V}}$) were determined:

$$[\boldsymbol{\sigma}'_{\mathrm{V}}] = [\mathbf{C}][\boldsymbol{\epsilon}'_{\mathrm{V}}] \text{ or}$$

$$\begin{bmatrix} \sigma'_{xx} \\ \sigma'_{yy} \\ \sigma'_{zz} \\ \sigma'_{yz} \\ \sigma'_{zx} \\ \sigma'_{xy} \end{bmatrix} = \begin{bmatrix} C_{11} & C_{12} & C_{12} & 0 & 0 & 0 \\ C_{12} & C_{11} & C_{12} & 0 & 0 & 0 \\ C_{12} & C_{12} & C_{11} & 0 & 0 & 0 \\ 0 & 0 & 0 & C_{44} & 0 & 0 \\ 0 & 0 & 0 & 0 & C_{44} & 0 \\ 0 & 0 & 0 & 0 & 0 & C_{44} \end{bmatrix} \begin{bmatrix} \epsilon'_{xx} \\ \epsilon'_{yy} \\ \epsilon'_{zz} \\ 2\epsilon'_{yz} \\ 2\epsilon'_{zx} \\ 2\epsilon'_{xy} \end{bmatrix}, \tag{7}$$

where C_{11}, C_{12} and C_{44} are the only independent stiffness coefficients of f.c.c. crystal structures. C_{11}, C_{12} and C_{44} for rock salt are 49, 13 and 13 GPa, respectively (Ahrens, 1995; Liu & He, 2007). The stress matrices of the grains ($\boldsymbol{\sigma}'$) were then reconstructed from $\boldsymbol{\sigma}'_{\mathrm{V}}$:

$$\boldsymbol{\sigma}' = \begin{bmatrix} \sigma'_{xx} & \sigma'_{xy} & \sigma'_{zx} \\ \sigma'_{xy} & \sigma'_{yy} & \sigma'_{yz} \\ \sigma'_{zx} & \sigma'_{yz} & \sigma'_{zz} \end{bmatrix}. \quad (8)$$

Having $\boldsymbol{\sigma}'$ of the grains, we can acquire the stresses of the grains in the specimen coordinate system ($\boldsymbol{\sigma}$) by employing the orientation matrices of the grains [equation (9)]:

$$[\boldsymbol{\sigma}] = [\mathbf{R}^{\mathrm{T}}][\boldsymbol{\sigma}'][\mathbf{R}]. \quad (9)$$

To evaluate the distribution of the stresses within the grains visually, the sub-volume of the specimens scanned by 3DXRD [Fig. 4(*b*)] was divided into a 3D fine mesh grid, where the stresses of each grid were interpolated from the nearest grain to the grid. Figs. 7(*a*)–7(*e*) show the evolution of σ_{zz} of the specimen No. 1 grains at different global ϵ_{zz}, whereas Figs. 7(*g*)–7(*l*) depict the evolution of σ_{zz} of the specimen No. 2 grains at various global ϵ_{zz}. Both specimens exhibited a consistent evolution of σ_{zz} within the grains with increasing global ϵ_{zz}. The trend matches the observation from the measured global σ_{zz}, showing that both specimens began to develop columns of grains transferring the axial stresses across their heights. Additionally, σ_{zz} began concentrating in specific parts of the specimens. These parts of the specimens, which were under higher axial stresses, had the potential to deform more than the rest of the specimen. The presence of differential deformation within the specimens eventually can lead to the propagation of cracks at the grain boundaries. Figs. 7(*c*)–7(*e*) show that specimen No. 1 grains located in the negative *y*-axis space experienced a much higher σ_{zz}. Coincidentally, the crown-shaped edges of specimen No. 1 were longer in the positive *y* direction [Fig. 7(*f*), which shows the volume rendering of specimen No. 1]. The longer edges on the positive *y* direction were crushed under high stresses, preventing the complete evolution of σ_{zz} in the grains located within the positive *y*-direction space. Meanwhile, σ_{zz} was distributed uniformly within specimen No. 2, which had a uniform edge at both ends. The spatial location of the grains with a high σ_{zz} (Fig. 7) demonstrates that no clear force columns or structures form during this loading condition. Instead, the highly stressed grains and regions are randomly distributed within the material.

Fig. 8 depicts the distribution of stresses within the grains of each specimen. The σ_{zz} distribution of the grains within specimen Nos. 1 and 2 showed a clear increase of 20 and 30 MPa in the mean σ_{zz}, respectively, at the end of the experiments. On the other hand, the distribution of the rest of the independent components of the $\boldsymbol{\sigma}$ tensors of the grains did not exhibit any significant changes during the experiments. This observation confirms that the global stresses applied to the specimens by the top loading platen are carried almost entirely vertically without forming any major force columns in the other directions. Figs. 8(*a*) and 8(*f*) show the distribution of the stresses within the specimens after the preparation. The mean values of shear components of the σ tensors of the grains (σ_{XY}, σ_{XZ} and σ_{YZ}) were zero. σ_{XY}, σ_{XZ} and σ_{YZ} were obtained from the 3DXRD measurements directly and

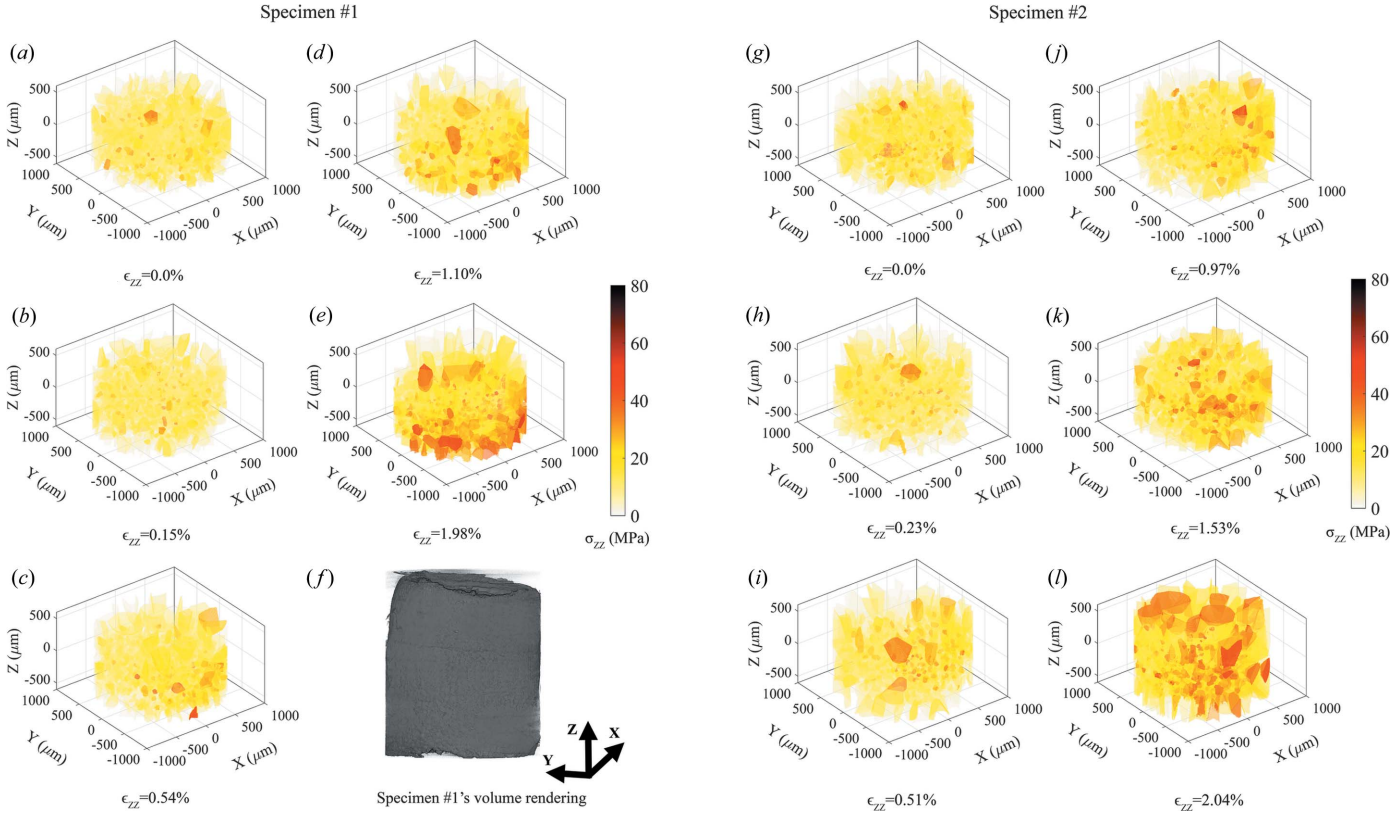

Figure 7
The changes in σ_{zz} within grains at different global axial strains: (*a*)–(*f*) specimen No. 1; (*g*)–(*l*) specimen No. 2.

represent the shear strains of the grains in the three orthogonal Cartesian directions of the specimens. The shear components of the $\boldsymbol{\sigma}$ tensors are absent because of the symmetry of the specimens and because the specimens are at equilibrium. However, the presence of the normal components of the $\boldsymbol{\sigma}$ tensors after the specimen preparation demonstrates the presence of residual normal lattice strains within the grains after the preparation. The mean values of σ_{XX}, σ_{YY} and σ_{ZZ} within grains were about +10 MPa, meaning that the scanned grains which were located in the center of the specimens were under tension. The specimens were immediately removed from the oven after the annealing and were cooled by being exposed to air at room temperature (20°C). The exposure to a temperature difference of about 180°C leads to a temperature shock. Therefore, the grains closer to the surface of the specimens cooled faster than the grains closer to the center of the specimens, leaving the grains closer to the center under tension. This observation shows that rock salt grains located closer to the surface and the grains closer to the center can easily develop compressional and tensional normal stresses, respectively, when exposed to a temperature shock.

Plastic deformations can only occur when the applied resolved shear stress (RSS) along at least one of the 24 slip systems reaches the critical resolved shear stresses (CRSS) on that specific slip system. The CRSS of each slip system increases as the stresses applied to the grains increase and the grains experience strain hardening. Although the values of CRSS depend on the stress history of a grain, still by comparing the RSS of the grains with the initial value of CRSS on a slip system, the activity of that slip system can be examined. The initial CRSS values, meaning there has been no strain hardening, for rock salt at room temperature under strain rates $\sim 10^{-4}$ s^{-1} in order for the $\{110\}\langle 1\bar{1}0\rangle$ ($\mathrm{CRSS}_{\{110\}}$), $\{100\}\langle 011\rangle$ ($\mathrm{CRSS}_{\{100\}}$) and $\{111\}\langle 1\bar{1}0\rangle$ ($\mathrm{CRSS}_{\{111\}}$) slip systems to be present are 5, 25 and 20 MPa, respectively (Carter & Heard, 1970). The RSS of the grains along each individual slip direction can be calculated from the stress matrices of the grains in their own coordinate system ($\boldsymbol{\sigma}'$) using equation (10):

$$\mathrm{RSS} = [\mathbf{d}] \cdot [\boldsymbol{\sigma}'] \cdot [\mathbf{n}], \tag{10}$$

where **d** is the direction of the slip and **n** is the unit normal vector to the slip plane. The calculated RSS of each individual grain was compared with the set of the initial CRSS of the slip systems to determine if each specific slip system could have been activated within the grain at any strain step. Fig. 9 shows the number of grains that had the chance to deform plastically on different potentially activated slip systems at any given global axial strain step. Initially, more than 87% of the grains of the specimens showed at least one potentially activated slip system. Therefore, a significant amount of plastic deformation occurred within the grains during the preparation of the

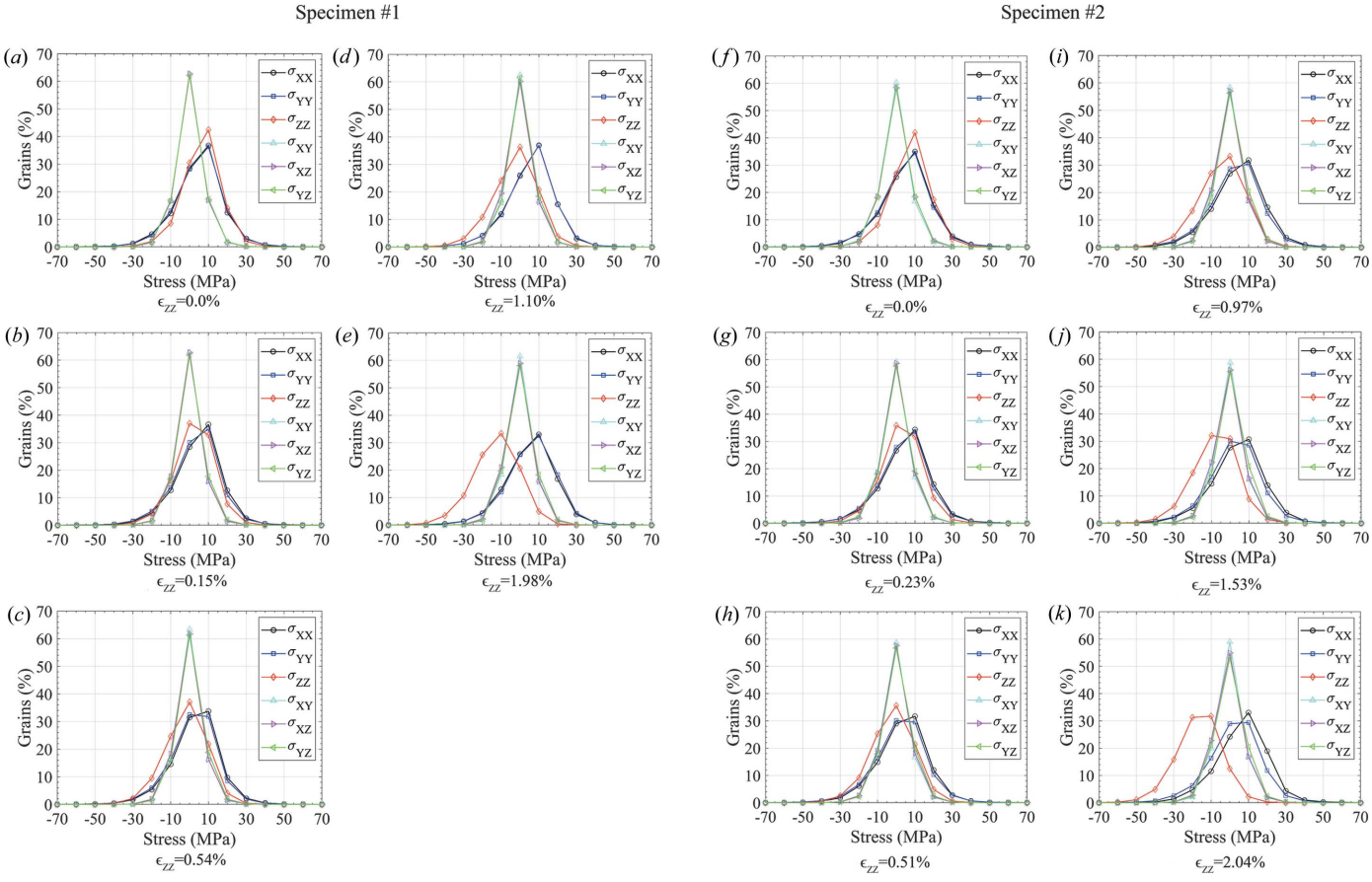

Figure 8
Distribution of stresses within grains at different global axial strains: (*a*)–(*e*) specimen No. 1; (*f*)–(*k*) specimen No. 2.

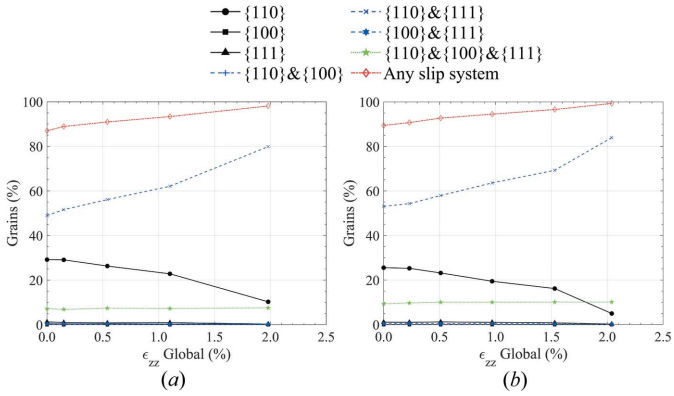

Figure 9
Percentage of the grains surpassing initial CRSS on different slip systems at any given global axial strain. (*a*) Specimen No. 1, (*b*) specimen No. 2.

specimens. More than 25% of the grains could only potentially slip on the {110}⟨1$\bar{1}$0⟩ slip system, while about 25% of the grains had the potential to slip on both {110}⟨1$\bar{1}$0⟩ and {111}⟨1$\bar{1}$0⟩ slip systems. Additionally, less than 10% of the grains exhibited RSS on all three slip systems, surpassing the corresponding initial CRSS values. We reiterate that the calculated RSS values are based on the remaining lattice strains within the individual grains. Therefore, these RSS values represent the locked-in stresses within the grains after the specimen preparation process due to the tension caused by thermal shock. To compare the RSS values with the CRSS values of the grains after strain hardening occurs within the grains, a matching algorithm similar to the algorithm developed by Amirrahmat *et al.* (2020) is needed to trace individual grains at each global axial strain step. The strain or stress tensor of each individual grain at each global axial strain step can then be compared with its initial value to obtain the strain or stress history of the grain. This history can then be utilized to evaluate the stress state of the grain and compare the RSS values with the respective CRSS values at any stress state. However, in the case of polycrystalline rock salt composed of fine grains, the resolution of an SMT scanner is not sufficient to obtain the precise spatial location of each individual grain needed for a matching algorithm.

The texture of the specimens after the preparation, which exhibited the strong presence of the {111} texture [Figs. 6(*a*) and 6(*f*)], shows that the approximately 25% of the grains that had the potential to slip on both {110}⟨1$\bar{1}$0⟩ and {111}⟨1$\bar{1}$0⟩ slip systems indeed slipped on the {111}⟨1$\bar{1}$0⟩ slip system. The RSS values of the grains after the specimen preparation illustrate that, under the high axial stresses applied to the specimens during the preparation (∼200 MPa), the {111}⟨1$\bar{1}$0⟩ slip system which has an initial CRSS value four times that of the initial CRSS of the {110}⟨1$\bar{1}$0⟩ slip system can be activated even at room temperature. The findings of previous studies (Ding *et al.*, 2016; Mills *et al.*, 2018; Moslehy & Alshibli, 2021) demonstrate that grain boundary migration, cataclasis, grain rotation, recrystallization and grain boundary diffusion are the

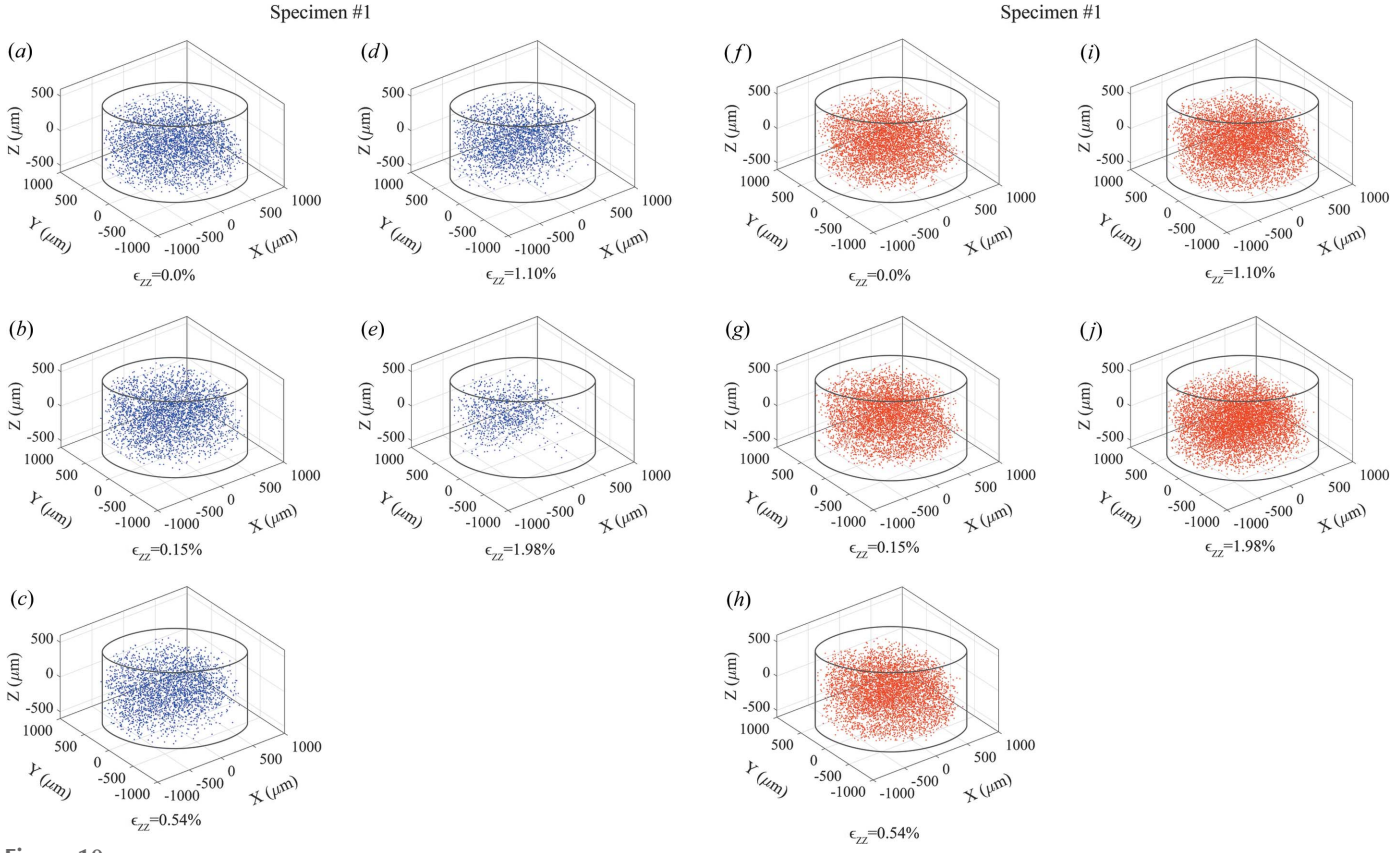

Figure 10
Location of the grains surpassing the initial CRSS on (*a*)–(*e*) {110}⟨1$\bar{1}$0⟩ and (*f*)–(*j*) {111}⟨1$\bar{1}$0⟩ slip systems for specimen No. 1.

main deformation mechanisms present during 1D compression loading of rock salt. However, the high values of RSS determined from the lattice strains occurring within the grains show that crystal plasticity contributes to the material deformations accumulated in 1D compression loading as well.

As the compression progressed, more than 98% of the grains within the specimens exhibited at least one activated slip system at the final 3DXRD scan. Moreover, the percentage of grains that could only slip on the $\{110\}\langle 1\bar{1}0\rangle$ slip system dropped to below 10% of the grains. On the other hand, the number of grains that had the potential to slip on both $\{110\}\langle 1\bar{1}0\rangle$ and $\{111\}\langle 1\bar{1}0\rangle$ slip systems increased to more than 80%. These changes in the potential slip systems agreed with the observations from the texture of the specimens, which showed a significant increase in the {111} texture with the increase of the stresses applied to the specimens (Fig. 6). Although the increase in the number of grains that had the potential to slip on both $\{110\}\langle 1\bar{1}0\rangle$ and $\{111\}\langle 1\bar{1}0\rangle$ slip systems started with the increase in the applied global σ_{zz}, the decrease in the number of grains that could slip only on the $\{110\}\langle 1\bar{1}0\rangle$ slip system did not occur until the applied global σ_{zz} reached 10 MPa. As mentioned earlier, the number of grains that showed at least one active slip system increased as soon as the experiments started. A hasty inference could be that the new grains that exhibited the potential to slip on any slip system had the potential to slip on both $\{110\}\langle 1\bar{1}0\rangle$ and $\{111\}\langle 1\bar{1}0\rangle$ slip systems. However, a deeper look at the initial CRSS values of the different slip systems shows that, at room temperature, the chances of the RSS of the $\{111\}\langle 1\bar{1}0\rangle$ slip system surpassing the initial CRSS before the RSS of the $\{110\}\langle 1\bar{1}0\rangle$ slip system surpasses its initial CRSS is marginal. In fact, the new grains that could slip on at least one slip system had the chance to slip on the $\{110\}\langle 1\bar{1}0\rangle$ slip system, and the grains that initially had the potential to slip on the $\{110\}\langle 1\bar{1}0\rangle$ slip system could then slip on both $\{110\}\langle 1\bar{1}0\rangle$ and $\{111\}\langle 1\bar{1}0\rangle$ slip systems, although $\{110\}\langle 1\bar{1}0\rangle$ was still found to be the dominant slip system.

Figs. 10 and 11 depict the location of the grains that had the potential to deform plastically on the $\{110\}\langle 1\bar{1}0\rangle$ slip system [Figs. 10(*a*)–10(*e*) for specimen No. 1 and Figs. 11(*a*)–11(*f*) for specimen No. 2] and the grains that could slip on both $\{110\}\langle 1\bar{1}0\rangle$ and $\{111\}\langle 1\bar{1}0\rangle$ slip systems [Figs. 10(*f*)–10(*j*) for specimen No. 1 and Figs. 11(*g*)–11(*l*) for specimen No. 2] throughout the experiments. The grains of specimen No. 1 that were located in the negative *y* direction showed a higher conversion from the potential to slip only on the $\{110\}\langle 1\bar{1}0\rangle$ slip system to the potential to slip on both $\{110\}\langle 1\bar{1}0\rangle$ and $\{111\}\langle 1\bar{1}0\rangle$ slip systems compared with the grains located in the positive *y* direction. This observation illustrates once again how the uneven crown-shaped edges of specimen No. 1 influenced the stresses transmitted to individual grains. The grains located in the negative *y* direction experienced higher axial stresses in the *z* direction due to the earlier development of the force columns in their region. Specimen No. 2, on the other hand, exhibited an entirely random distribution of the

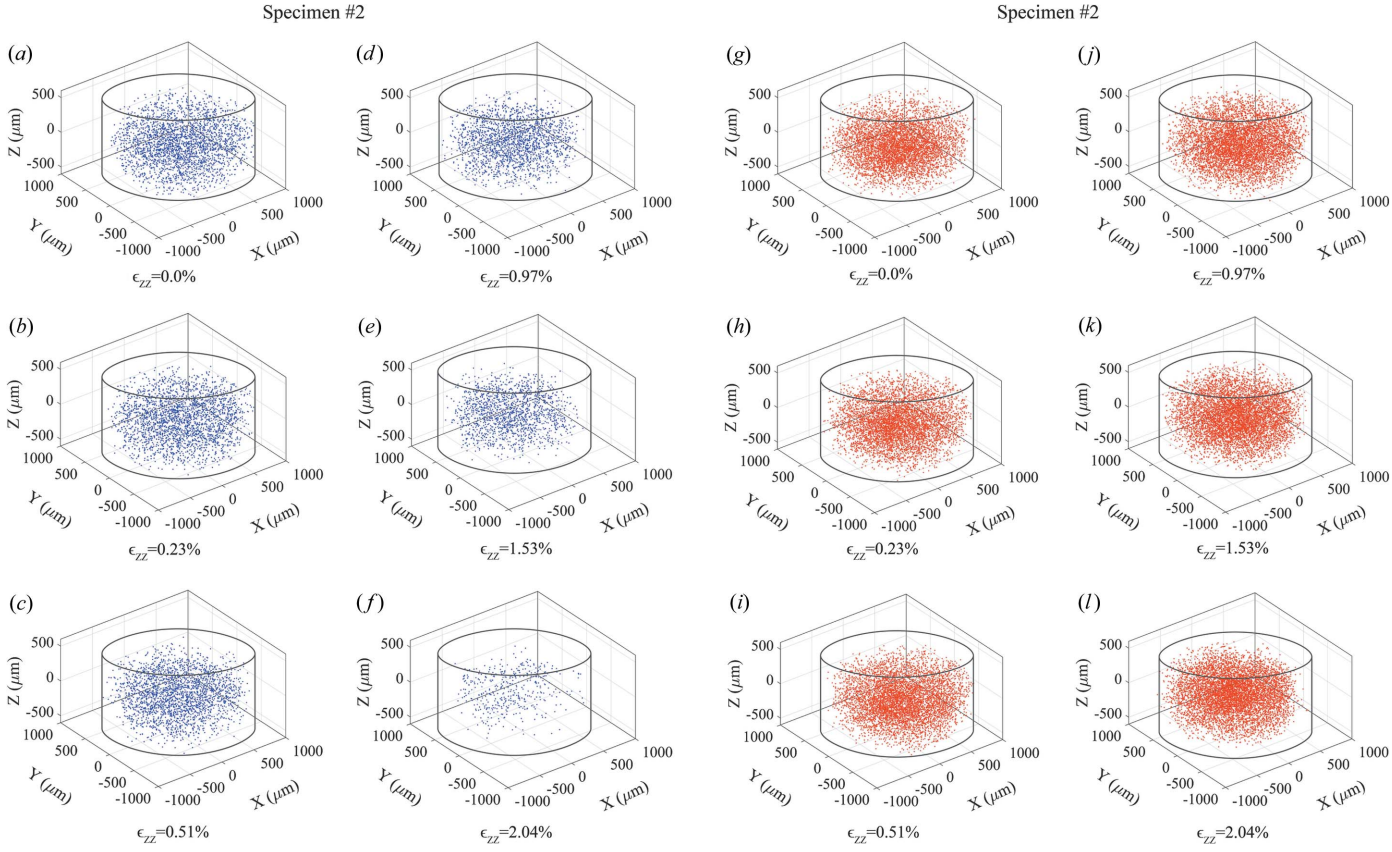

Figure 11
Location of the grains surpassing the initial CRSS on (*a*)–(*f*) $\{110\}\langle 1\bar{1}0\rangle$ and (*g*)–(*l*) $\{111\}\langle 1\bar{1}0\rangle$ slip systems for specimen No. 2.

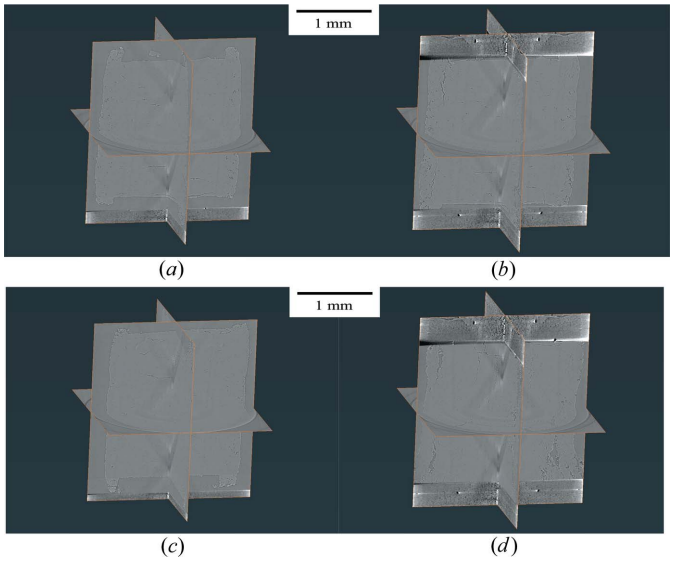

Figure 12
The SMT scans of specimen No. 1 (*a*) at the initial state ($\epsilon_{zz} = 0.0\%$) and (*b*) at the end of the test ($\epsilon_{zz} = 1.98\%$); and specimen No. 2 (*c*) at the initial state ($\epsilon_{zz} = 0.0\%$) and (*d*) at the end of the test ($\epsilon_{zz} = 3.32\%$).

grains having the $\{110\}\langle 1\bar{1}0\rangle$ slip system and both the $\{110\}\langle 1\bar{1}0\rangle$ and $\{111\}\langle 1\bar{1}0\rangle$ slip systems activated throughout the experiment.

3.3. The evolution of the crack networks

Fig. 12 depicts the reconstructed 3D images of the specimens before the unconfined compression tests and after the tests. To identify the crack network within the specimens each reconstructed 3D image was first filtered by an anisotropic diffusion filter using *Avizo* (FEI, 2018) to remove the instrumental noise within the image. The image was then thresholded to separate the pores and cracks from the rest of the medium. Fig. 12 shows x-shaped artifacts within all reconstructed 3D images, caused by the existence of the apparatus' four acrylic rods, which adversely influenced both the segmented crack networks of the specimen and the calculated porosity. These x-shaped artifacts were mostly removed from the SMT scans using *Avizo*'s interactive and hysteresis thresholding modules. Ring artifacts are another common type of artifact in CT images, which were observed in the collected SMT scans (as seen later in Fig. 13). Since ring artifacts follow a perfect 2D circle shape, the equation of the

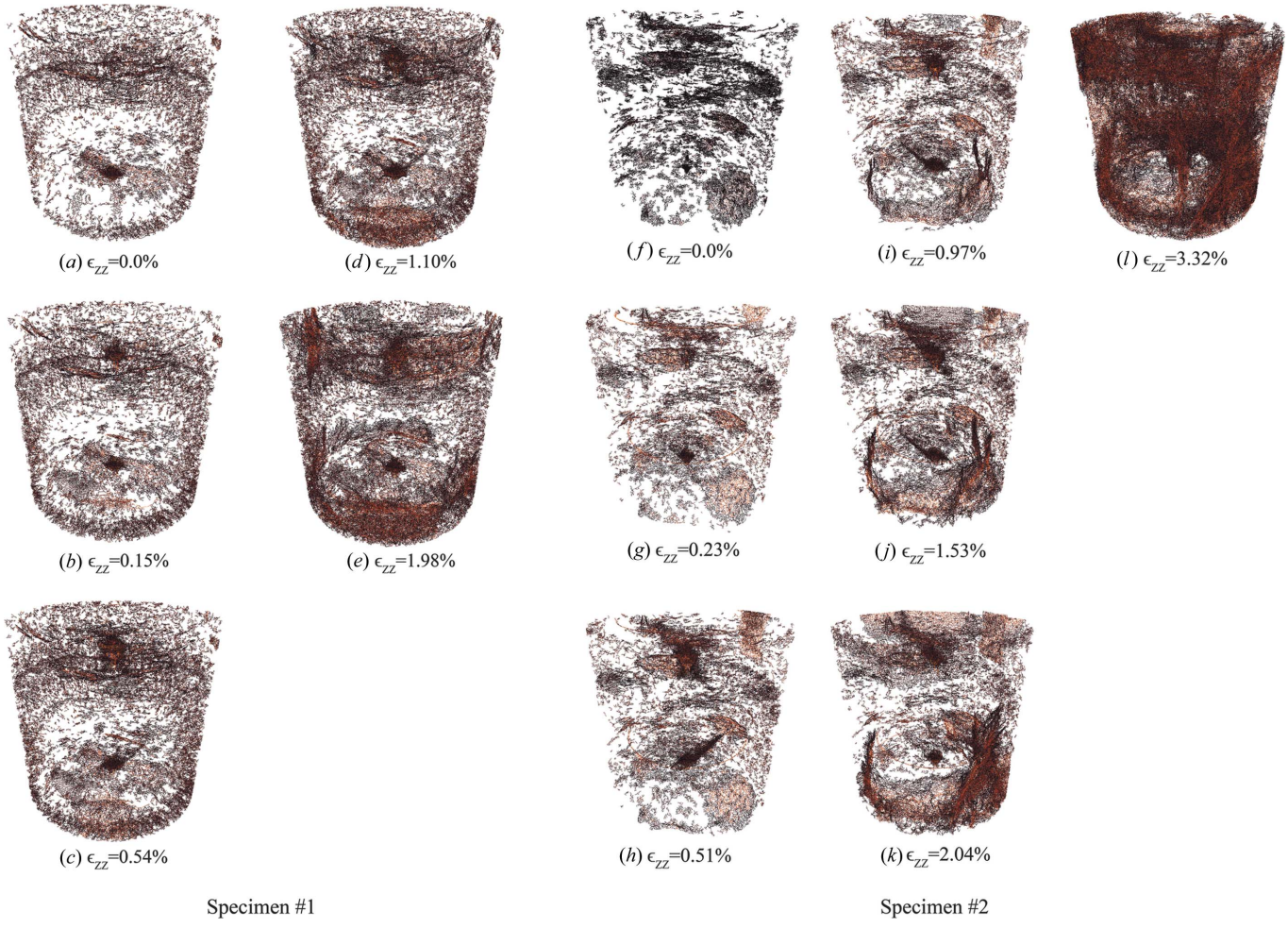

Figure 13
The evolution of cracks within the specimens at different global axial strain steps: (*a*)–(*e*) specimen No. 1; (*f*)–(*l*) specimen No. 2.

governing circle of each ring artifact can be found within the affected scans using *Avizo*'s inspection and measuring tools. The identified ring artifacts were then removed from the segmented images using *Avizo*'s 'Not' module. Once the mentioned artifacts had been remedied, the separated pores within the specimens with a volume of less than 3000 μm^3 were found and removed from the image because they were not part of any locally connected pore (crack) network within the specimens. The locally connected pore network within the specimens at each strain level was generated to investigate the evolution of the crack networks with loading (Fig. 13).

Both specimens had some pre-developed local crack networks prior to the tests and exhibited a dome-shaped, pre-developed crack as shown in Figs. 13(*a*) and 13(*f*). As noted before, the specimens were prepared in three equal-height layers, and these dome-shaped, horizontally oriented crack networks show pores at the boundaries of the different layers. In other words, the boundaries of these layers were not fully integrated. These horizontally oriented crack networks did not develop further and gradually decreased in size as the applied global stresses increased. The evolution of the cracks up to global axial strains of about 0.50% did not have any preferred orientation. Cracks can normally occur along grain boundaries or as a result of cracks forming within grains. Moreover, because the grains of the specimens were smaller than the resolution of the SMT scans, the cracks formed within the grains could not be detected, and all the cracks shown in the images were a result of the cracks formed at the grain boundaries. Grain boundaries depending on the condition in which they have been formed are usually weaker than the grains themselves. As a result, cracks along the grain boundaries are more likely to form under lower applied stresses. Therefore, up to 0.50% global axial strain (σ_{zz} of about 10 MPa) the cracks had been developing along the grain boundaries, which did not necessarily follow any specific texture or direction.

The cracks formed after the global axial strains of about 0.50% gradually became vertical and started developing locally connected crack networks in the z direction. Looking back at Fig. 8, the grains only exhibited a significant increase in σ_{zz} compared with the other components of the σ tensors. These vertical cracks were more prominent far from the specimens' axes where the lateral support by the specimen itself is much lower. The vertical cracks formed within specimen No. 1 had a stronger presence in the parts of the specimen located in the positive y direction [Fig. 13(*e*)]. As seen in Fig. 10(*e*), the grains located in the positive y direction of specimen No. 1 mainly showed higher activities on the $\{110\}\langle 1\bar{1}0\rangle$ slip system compared with the grains located in the negative y direction. The initial CRSS of the $\{110\}\langle 1\bar{1}0\rangle$ slip system is much lower than that of the $\{111\}\langle 1\bar{1}0\rangle$ slip system. Therefore, the grains slipping on the $\{110\}\langle 1\bar{1}0\rangle$ slip system could exhibit higher plastic deformations, which could eventually lead to the development of intra- and inter-grain cracks. Fig. 13(*l*) shows a substantial increase in the development of the crack network within specimen No. 2. As seen in Fig. 5, specimen No. 2 at this stage experienced significant plastic deformations, which caused the greater evolution of the crack network within specimen No. 2.

The SMT scans of the specimens were further analyzed to evaluate the existence of a fully connected crack network across the specimens at each global axial strain. Only specimen No. 2 at ϵ_{zz} = 3.32% showed a fully connected crack network across the specimen, which is illustrated in Fig. 14(*a*). Comparing Fig. 14(*a*) with Fig. 13(*l*) demonstrates that not all of the locally connected crack networks contributed to the development of the fully connected network within specimen No. 2 and some did not become part of it. The vertical cracks that developed closer to the surface of the specimen evolved into a fully connected crack network, while the horizontal cracks and the vertical cracks located closer to the cylindrical axis of the specimen were less involved in the fully connected crack network. The evolution of a fully connected crack network within specimen No. 2 in the z direction demonstrates that after undergoing ϵ_{zz} of 3.32% the specimen could become permeable, though only in the loading direction. On the other hand, the absence of a fully connected crack (pore) network within the specimens at the other global axial strain steps shows that the material up to ϵ_{zz} of 2.00% remains potentially impermeable.

The porosities of the specimens at each global axial strain were calculated from the volume of the pores (cracks) with respect to the total volume of the specimens. Fig. 14(*b*) shows the relationship between the porosities of the specimens (ϕ) and ϵ_{zz}. Neither specimen displayed a significant increase in its porosity up to ϵ_{zz} of about 2.00%. As discussed before, the specimens also did not exhibit a spike in the development of the crack networks up to this stage. Therefore, it is safe to deduce that the porosity of rock salt remains small below an ϵ_{zz} of about 2.00% (corresponding to σ_{zz} of about 30 MPa). Although not significant, a direct increase in the porosities of the specimens was observed with the increase in the applied ϵ_{zz}. If the applied global σ_{zz} exceeds the critical value of 30 MPa, the material eventually evolves a fully connected crack network in the z direction, which significantly increases the permeability of the material in the z direction. Therefore, global σ_{zz} higher than 30 MPa can be detrimental to the stability and serviceability of rock salt caverns possessing a similar initial texture and porosity to the specimens studied in

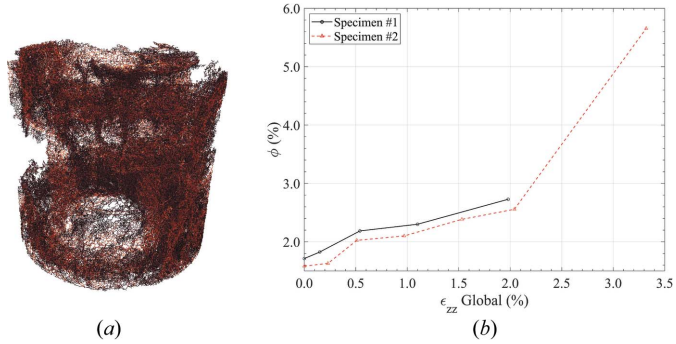

(*a*) (*b*)

Figure 14
(*a*) The connected crack network within specimen No. 2 at 3.32% strain; (*b*) porosity of the specimens at different global axial strains.

this paper. Porous rock salt under unconfined compression loading generally shows an initial contraction (caused by the closure of the cracks and pores within the medium) followed by a continuous expansion until failure. However, the specimens tested in this study exhibited a continuous expansion throughout the tests. They were prepared at a uniaxial stress of 200 MPa and possessed a low initial porosity, which reduced their potential to show contraction at the beginning of the experiments. Moreover, significant closure of the cracks within the specimens was not observed in the SMT scans obtained throughout the experiments (Fig. 13). Specimen No. 2 showed a spike in ϕ at the final global axial strain step (3.32%), where it possessed a fully connected crack network. The porosity of specimen No. 2 at this step (ϕ = 5.7%) surpassed the upper limit of the critical ϕ value (5%) suggested by Paneru *et al.* (2018), which corresponds to the porosity of rock salt where it becomes permeable. Conversely, the specimens under ϵ_{zz} of more than 0.50% surpassed the lower limit of the critical ϕ value (2%), although they did not demonstrate a fully connected crack network. The discrete scanning nature of *in situ* 3DXRD and SMT limited the number of steps at which the specimens could be scanned in a timely manner. As a result, the critical ϕ where the specimens evolved a fully connected crack network remains unknown. However, based on the SMT scans obtained at ϵ_{zz} of about 2.00 and 3.32%, the critical ϕ of the specimens could range between 2.5 and 5.7%.

4. Summary and conclusions

Two small-scale polycrystalline specimens were prepared at 200 MPa uniaxial stress inside an acrylic die. The specimens were then tested under the unconfined compression procedure coupled with *in situ* SMT and 3DXRD scanning. The SMT and 3DXRD scans in conjunction with the global stress–strain measurements from the tests were analyzed to investigate the evolution of texture, internal stresses, cracks and porosity of the specimens initially and at different strain steps during the unconfined compression tests. A preferred texture along the {111} orientation was observed after the specimen preparation under the 1D compression loading and annealing. More than 87% of the grains potentially had deformed plastically during the preparation process, showing that a significant amount of crystal plasticity occurs during the 1D compression of the material. The dominant slip system was identified as {110}$\langle 1\bar{1}0\rangle$ at this stage. The only pre-existing crack networks were dome-shaped crack networks oriented horizontally and located at the boundaries of the different layers by which the specimens were prepared, which shows the boundaries of these layers were not fully diffused. On the other hand, the porosity of the material was about 1.6% and it did not possess a fully connected crack network after the preparation, pointing to low permeability of the material.

During the unconfined compression test, the specimens developed a stronger texture along the {111} orientation, and the other textures diminished with the increases of global axial strain. As the applied stresses increased, the grains showed more activity on the {111}$\langle 1\bar{1}0\rangle$ slip system and the activity of the {110}$\langle 1\bar{1}0\rangle$ slip system was decreased, showing that, within polycrystalline rock salt with an initially strong {111} texture, the {111}$\langle 1\bar{1}0\rangle$ slip system can become more dominant than in polycrystalline rock salt with a random initial texture. No clear force chain or structure formation was observed during the tests.

Under global axial strains up to about 0.50% (corresponding to global axial stresses of about 10 MPa), the specimens showed development of local crack networks in all directions. The porosity of the material was still under 2% and no fully connected crack network was observed. However, surpassing global axial strains of about 0.50%, the crack networks started to develop mainly in the z (loading) direction, although fully connected crack networks throughout the material were not formed. This means the material can still be considered as nearly impermeable. Reaching a global axial strain of 3.32% (corresponding to global axial stresses of about 30 MPa) and porosity of 5.7% a fully connected crack network was found, indicating a potential increase in the permeability of the material.

Acknowledgements

Any opinions, findings, conclusions, and recommendations expressed in this material are those of the authors and do not necessarily reflect the views of the National Science Foundation. P-XRD was carried out at the Joint Institute for Advanced Materials (JIAM) Diffraction Facility of the University of Tennessee, Knoxville. The SMT and 3DXRD images were collected using beamline 1-ID at Argonne Photon Source, Argonne National Laboratory. The authors thank Dr Siavash Amirrahmat, Isabella Alamilla and Darcie Halliburton, undergraduate research assistants at the University of Tennessee, Knoxville, for their help.

Funding information

This material is based on work supported by the National Science Foundation under grant No. CMMI-1641054. Use of the Advanced Photon Source, an Office of Science User Facility operated for the US Department of Energy (DOE) Office of Science by Argonne National Laboratory, was supported by the US DOE under contract No. DE-AC02-06CH11357.

References

Ahrens, T. J. (1995). *Mineral Physics and Crystallography: a Handbook of Physical Constants*. Washington, DC: American Geophysical Union.
Alkan, H. (2009). *Int. J. Rock Mech. Min. Sci.* **46**, 716–724.
Alshibli, K., Cil, M. B., Kenesei, P. & Lienert, U. (2013). *Granul. Matter*, **15**, 517–530.
Amirrahmat, S., Imseeh, W. H., Alshibli, K. A., Kenesei, P., Jarrar, Z. A. & Sharma, H. (2020). *J. Geotech. Geoenviron. Eng.* **146**, 04020027.
ASTM (2015). D2850-15, *Standard Test Method for Unconsolidated-Undrained Triaxial Compression Test on Cohesive Soils*. ASTM International, West Conshohocken, PA, USA.
ASTM (2019). D2216-19, *Standard Test Methods for Laboratory Determination of Water (Moisture) Content of Soil and Rock by*

Mass. ASTM International, West Conshohocken, PA, USA, https://doi.org/10.1520/D2216-19.
ASTM (2020). D4767-11, *Standard Test Method for Consolidated Undrained Triaxial Compression Test for Cohesive Soils*. ASTM International, West Conshohocken, PA, USA.
Bauer, S. & Urquhart, A. (2016). *Acta Geotech.* **11**, 913–924.
Black, D. R., Windover, D., Henins, A., Filliben, J. & Cline, J. P. (2011). *Powder Diffr.* **26**, 155–158.
Borthwick, V. E., Schmidt, S., Piazolo, S. & Gundlach, C. (2012). *Geochem. Geophys. Geosyst.* **13**, Q05005.
Borthwick, V., Schmidt, S., Piazolo, S., Gundlach, C., Griera, A., Bons, P. D. & Jessell, M. W. (2012). *Mater. Sci. Forum*, **715–716**, 461–466.
Carter, N. L. & Heard, H. C. (1970). *Am. J. Sci.* **269**, 193–249.
Carter, N. L., Horseman, S. T., Russell, J. E. & Handin, J. (1993). *J. Struct. Geol.* **15**, 1257–1271.
Chen, J., Peng, H., Fan, J., Zhang, X., Liu, W. & Jiang, D. (2020). *RSC Adv.* **10**, 2877–2886.
Cosenza, P., Ghoreychi, M., Bazargan-Sabet, B. & de Marsily, G. (1999). *Int. J. Rock Mech. Min. Sci.* **36**, 509–526.
Degen, T., Sadki, M., Bron, E., König, U. & Nénert, G. (2014). *Powder Diffr.* **29**, S13–S18.
Ding, J., Chester, F. M., Chester, J. S., Zhu, C. & Arson, C. (2016). *50th US Rock Mechanics/Geomechanics Symposium*. Alexandria: ARMA.
Ding, W., Li, H., Pfeifer, P. & Dittmeyer, R. (2014). *Chem. Eng. J.* **254**, 545–558.
Druckrey, A. M. & Alshibli, K. A. (2016). *Int. J. Numer. Anal. Methods Geomech.* **40**, 105–116.
Fam, M., Santamarina, J. C. & Dusseault, M. B. (1998). *J. Environ. Eng. Geophys.* **3**, 15–26.
FEI (2018). *Avizo 9.7*. FEI Visualization Sciences Group, Hillsboro, OR, USA.
Habibi, R. (2019). *Oil Gas Sci. Technol. IFP Energies Nouv.* **74**, 14.
Hielscher, R. & Schaeben, H. (2008). *J. Appl. Cryst.* **41**, 1024–1037.
Hurley, R. C., Hall, S. A., Andrade, J. E. & Wright, J. (2016). *Phys. Rev. Lett.* **117**, 098005.
Hurley, R. C., Herbold, E. B. & Pagan, D. C. (2018). *J. Appl. Cryst.* **51**, 1021–1034.
Imseeh, W. H. & Alshibli, K. A. (2018). *Comput. Geotech.* **94**, 184–195.
Imseeh, W. H., Alshibli, K. A., Moslehy, A., Kenesei, P. & Sharma, H. (2020). *Comput. Geotech.* **126**, 103718.
Keller, L. M., Jobmann, M., Schuetz, P. & Gasser, P. (2014). *Transp. Porous Media*, **104**, 607–620.
Lebensohn, R. A., Dawson, P. R., Kern, H. M. & Wenk, H.-R. (2003). *Tectonophysics*, **370**, 287–311.
Linckens, J., Zulauf, G. & Hammer, J. (2016). *J. Geophys. Res. Solid Earth*, **121**, 6150–6171.
Liu, Q. & He, Q. (2007). *Acta Phys. Pol. A*, **112**, 69–76.
Liu, W., Zhang, Z., Chen, J., Fan, J., Jiang, D., Jjk, D. & Li, Y. (2019). *Energy*, **185**, 682–694.
Liu, Y., Gilormini, P. & Ponte Castañeda, P. (2005). *Tectonophysics*, **406**, 179–195.
McCusker, L. B., Von Dreele, R. B., Cox, D. E., Louër, D. & Scardi, P. (1999). *J. Appl. Cryst.* **32**, 36–50.
Mills, M. M., Stormont, J. C. & Bauer, S. J. (2018). *Eng. Geol.* **239**, 206–213.
Moslehy, A. & Alshibli, K. (2021). *J. Rock Mech. Geotech. Eng.* **13**, 311–320.
Na, S. & Sun, W. (2018). *Comput. Methods Appl. Mech. Eng.* **338**, 657–691.
Paneru, L. P., Bauer, S. J. & Stormont, J. C. (2018). *Rock Mech. Rock Eng.* **51**, 911–923.
Popp, T., Kern, H. & Schulze, O. (2001). *J. Geophys. Res.* **106**, 4061–4078.
Rivers, M. L. (2012). *Proc. SPIE*, **8506**, 169–181.
Schulze, O., Popp, T. & Kern, H. (2001). *Eng. Geol.* **61**, 163–180.
Senseny, P. E., Hansen, F. D., Russell, J. E., Carter, N. L. & Handin, J. W. (1992). *Int. J. Rock Mech. Min. Sci. Geomech. Abs.* **29**, 363–378.
Sharma, H., Huizenga, R. M. & Offerman, S. E. (2012*a*). *J. Appl. Cryst.* **45**, 693–704.
Sharma, H., Huizenga, R. M. & Offerman, S. E. (2012*b*). *J. Appl. Cryst.* **45**, 705–718.
Singh, A., Kumar, C., Gopi Kannan, L., Seshagiri Rao, K. & Ayothiraman, R. (2018). *Eng. Geol.* **243**, 218–230.
Skrotzki, W. & Welch, P. (1983). *Tectonophysics*, **99**, 47–61.
Staudtmeister, K. & Rokahr, R. B. (1997). *Int. J. Rock Mech. Min. Sci.* **34**, 300-e1–300-e13.
Sun, Z., Fan, J., Wu, F. & Chen, J. (2019). *Therm. Sci.* **23**, 997–1003.
Swanson, H. E. & Fuyat, R. K. (1953). *Natl. Bur. Stand.* **539**, 41–43.
Talbot, C. J. (1978). *Nature*, **273**, 739–741.
Thiemeyer, N., Habersetzer, J., Peinl, M., Zulauf, G. & Hammer, J. (2015). *J. Struct. Geol.* **77**, 92–106.
Toby, B. H. & Von Dreele, R. B. (2013). *J. Appl. Cryst.* **46**, 544–549.
Viganò, N. & Ludwig, W. (2018). *J. Instrum.* **13**, C04017.
Viganò, N., Tanguy, A., Hallais, S., Dimanov, A., Bornert, M., Batenburg, K. J. & Ludwig, W. (2016). *Sci. Rep.* **6**, 20618.
Wang, T. T., Ma, H. L., Shi, X. L., Yang, C. H., Zhang, N., Li, J. L., Ding, S. L. & Daemen, J. J. K. (2018). *Int. J. Rock Mech. Min. Sci.* **102**, 57–70.
Yin, H., Ma, H., Shi, X., Li, H., Ge, X. & Gao, A. (2019). *J. Cent. S. Univ.* **26**, 2185–2196.
Yin, H., Yang, C., Ma, H., Shi, X., Zhang, N., Ge, X., Li, H. & Han, Y. (2020). *Acta Geotech.* **15**, 549–563.
Zeljaś, D. (2016). *AGH Drilling Oil Gas*, **33**, 699–711.
Zhang, Q. Y., Duan, K., Jiao, Y. Y. & Xiang, W. (2017). *Int. J. Rock Mech. Min. Sci.* **94**, 43–54.
Zhu, C. & Arson, C. (2014). *Acta Geotech.* **9**, 847–867.